



21

ABSTRACT

22 Tides play an important role in ocean energy transfer and mixing, and provide major energy for
23 maintaining thermohaline circulation. This study proposes a new explicit tidal scheme and
24 assesses its performance in a global ocean model. Instead of using empirical specifications of
25 tidal amplitudes and frequencies, the new scheme directly uses the positions of the Moon and
26 Sun in a global ocean model to incorporate tides. Compared with the traditional method that has
27 specified tidal constituents, the new scheme can better simulate the diurnal and spatial
28 characteristics of the tidal potential of spring and neap tides as well as the spatial patterns and
29 magnitudes of major tidal constituents (K1 and M2). It significantly reduces the total errors of
30 eight tidal constituents (with the exception of N2 and Q1) in the traditional explicit tidal scheme.
31 Relative to the control simulation without tides, both the new and traditional tidal schemes can
32 lead to better dynamic sea level (DSL) simulation in the North Atlantic, reducing significant
33 negative biases in this region. The new tidal scheme also shows smaller positive bias than the
34 traditional scheme in the Southern Ocean. The new scheme is suited to calculate regional
35 distributions of sea level height in addition to tidal mixing.

36



37 **1. Introduction**

38 Diapycnal mixing plays a crucial role in the interior stratification of global oceans and
39 meridional overturning circulation. To sustain the mixing, a continuous supply of mechanical
40 energy is needed (Huang 1999; MacKinnon 2013). It has been suggested that the breaking of
41 internal tides is a major contribution to diapycnal mixing in deep seas (Wang et al., 2017),
42 whereas the breaking of internal waves generated by surface wind is a major source within the
43 upper ocean (Wunsch and Ferrari 2004). Through the analysis of observational data and
44 numerical model simulations, previous studies have shown that tides can provide about 1TW of
45 mechanical energy for maintaining the thermohaline circulation, accounting for about half of the
46 total mechanical energy (Egbert and Ray, 2003; Jayne and Laurent, 2001). Local strong tidal
47 mixing also affects ocean circulations on a basin scale. For instance, tidal mixing in both the
48 Luzon Strait and South China Sea has a pronounced impact on water mass properties and, in the
49 South China Sea, has intermediate–deep layer circulation features (Wang et al., 2017). Due to
50 interactions with sea ice, tidal mixing in the Arctic seas could modify the salinity budget, which
51 further affects the deep thermohaline circulation in the North Atlantic (Postlethwaite et al., 2011).
52 Therefore, it is necessary to fully consider the effects of tidal processes in state-of-the-art ocean
53 models.

54 Tides were omitted in the early ocean general circulation models (OGCMs) in which the
55 “rigid-lid” approximation is applied to increase the integration time steps of the barotropic
56 equation for computational efficiency, which filtered out the gravity waves including the tides.



57 Free surface methods were later introduced to ocean models (e.g., Zhang and Liang, 1989;
58 Killworth et al., 1991; Zhang and Endoh, 1992), but tides were often neglected since the focus of
59 many studies has been on the variations in large-scale ocean general circulations on much longer
60 time scales than tides. With the development of theories of ocean general circulations and the
61 recognition of the importance of tides on large-scale circulations, the effects of tides have begun
62 to be considered in OGCMs in the last twenty years.

63 The tidal processes are typically incorporated into OGCMs in two different ways. One is in
64 an implicit form and the other is in an explicit form. The implicit form uses an indirect
65 parameterization scheme that does not simulate the tides themselves (Laurent et al. 2002). It
66 enhances mixing, especially for deep seas and coastal areas, to represent the tidal effects. This
67 type of mixing scheme was first applied in a coarse-resolution OGCM by Simmons et al. (2004),
68 and their results show that the biases of ocean temperature and salinity are substantially smaller.
69 Saenko and Merryfield (2005) reported that this type of parameterization scheme contributes to
70 the amplification of bottom-water circulation especially for the Antarctic Circumpolar Current
71 and deep-sea stratification. Yu et al. (2017) pointed out that the tidal mixing scheme has a
72 significant effect on the simulation of the Atlantic meridional overturning circulation (AMOC)
73 intensity in OGCM. This parameterization type is mainly used for internal-tide generation, in
74 which the resultant vertical mixing is ad hoc, with an arbitrarily prescribed exponential vertical
75 decay (Melet et al., 2013).



76 The explicit form incorporates the tidal forcing into the barotropic equation of free-surface
77 OGCMs. The typical tidal forcing consists of four primary diurnal (K1, O1, P1 and Q1) and four
78 primary semidiurnal (M2, S2, N2 and K2) constituents. Each of the constituents is determined by
79 a prescribed amplitude, frequency and phase (Griffies et al. 2009). The explicit tidal forcing has
80 been implemented in several OGCMs in recent decades (Thomas et al., 2001; Zhou et al., 2002;
81 Schiller, 2004; Schiller and Fiedler, 2007; Müller et al., 2010). Arbic et al. (2010) reported the
82 first explicit incorporation of tides into an eddy-resolving OGCM that led to a drastic
83 improvement in the interaction between tides and mesoscale eddies.

84 The purpose of this study is to propose a new explicit tidal scheme in a CMIP6 class of
85 OGCMs (Phase 6 of the Coupled Model Intercomparison Project) and assess its performance.
86 The scheme is directly based on the actual position of the Sun and Moon relative to the Earth and
87 calculates precise gravitational tidal forcing instead of applying the empirical constants of tidal
88 amplitudes and frequencies.

89 The structure of this paper is as follows: the new explicit tidal scheme is introduced in
90 section 2. The model configuration, numerical experiment design and data used in this study are
91 described in section 3. Section 4 presents the results of the numerical experiment. Section 5
92 contains a summary and discussion.

93 **2. The new explicit tidal forcing**

94 Tidal forcing is mainly the result of the combination of the gravitational pull exerted by the
95 Moon and Sun and inertial centrifugal forces generated by the Earth's rotation. First, we only



96 take the Moon as an example for simplicity (Fig. 1); the vertical tidal force can be ignored,
97 which is far less than the gravity, and is part of the force in the hydrostatic balance. Assuming
98 that the Earth is a rigid body, the horizontal tide-generating force is:

$$F_{tide,m} = \frac{GM_m}{L^2} \sin(\theta_m + r) - \frac{GM_m}{D_m^2} \sin \theta_m \quad (1)$$

99 where the first term on the right-hand side is the horizontal gravitational force at the surface, and
100 the second term is the horizontal gravitational force at the center that should be equal to the
101 inertial centrifugal force. G is the universal gravitation constant which can also be denoted as
102 $g \frac{a^2}{E}$, where E is the mass of the Earth, M_m is the mass of the moon, and θ_m is the zenith angle of
103 the Moon and an arbitrary position X on the Earth. $F_{tide,m}$ can be considered the deviation of the
104 horizontal gravitational force at the surface from that at the center of the Earth.

105 According to analytic geometry and the law of cosines, we can obtain:

$$\sin(\theta_m + r) = \frac{D_m \sin \theta_m}{L} \quad (2)$$

$$L^2 = D_m^2 + a^2 - 2aD_m \cos \theta_m \quad (3)$$

106 Based on the above three equations, equation (1) can be written as:

$$F_{tide,m} = \frac{3M_m}{2E} \left(\frac{a}{D_m} \right)^3 g \sin 2\theta_m \quad (4)$$

107 To compare with the traditional explicit tidal forcing formula of the eight most important
108 constituents of the diurnal and semidiurnal tides, the instantaneous tidal height (tidal potential)
109 due to equilibrium tides is diagnosed by the spatial integration of equation (4):

$$\eta_{tide,m} = \int_{\Theta}^{\theta_m} (F_{tide,m} \cdot a) d\theta_m \quad (5)$$

110 Where, Θ is the zenith angle of the zero potential energy surface. With the global total tidal
111 height at zero, $\cos^2 \Theta = 1/3$. Therefore, the instantaneous tidal height is:



$$\eta_{tide,m} = \frac{M_m}{E} \frac{a^4}{D_m^3} \frac{h}{2} (3\cos^2 \theta_m - 1) \quad (6)$$

112 where the love number h is introduced to represent the reduction in tidal forcing caused by the
 113 deformation of the solid Earth. It is usually set equal to 0.7 (Wahr, 1981; Griffies 2004), which is
 114 adopted here.

115 Therefore, the tidal potential after taking into account tidal forcing due to both the Moon
 116 and Sun is as follows:

$$\eta_{tide} = \frac{M_m}{E} \frac{a^4}{D_m^3} \frac{h}{2} (3\cos^2 \theta_m - 1) + \frac{M_s}{E} \frac{a^4}{D_s^3} \frac{h}{2} (3\cos^2 \theta_s - 1) \quad (7)$$

117 The zenith angle θ_m is calculated as follows:

$$\cos \theta_m = \sin \varphi \sin \varphi_m + \cos \varphi \cos \varphi_m \cos T_m \quad (8)$$

$$T_m = \begin{cases} \lambda_m - \lambda, & (\lambda_m - \lambda) \in [0, \pi] \\ \lambda_m - \lambda + 2\pi, & (\lambda_m - \lambda) \notin [0, \pi] \end{cases} \quad (9)$$

118 where φ and λ are the latitude and longitude of the position X on the Earth, respectively; φ_m and
 119 λ_m are the latitude and longitude of the projection point of the Moon on the Earth, respectively,
 120 and are both functions of universal time (Montenbruck and Gill, 2000). The zenith angle θ_s is
 121 similarly calculated.

122 Finally, explicit tidal forcing is introduced into the equation of barotropic mode motion:

$$\frac{\partial \vec{V}}{\partial t} = -\frac{1}{\rho_0} \nabla_h p_{as} - g' \nabla_h (\alpha \eta - \eta_{tide}) + \bar{P} + f \vec{k} \times \vec{V} + \tau_{tide} \quad (10)$$

123 where \vec{V} is the barotropic velocity, $\nabla_h = (\partial/\partial x, \partial/\partial y)$; p_{as} is the sea surface air pressure; $g' =$
 124 $g\rho/\rho_0$ and $\alpha = 0.948$ represent the self-attraction of the Earth and the correction generated by
 125 full self-attraction and loading (SAL) (Hendershott, 1972), which refers to the redistribution of
 126 the sea surface height between the Earth and the ocean due to the existence of tide-generating



127 potential. SAL treatment is a scalar approximation in order to make the calculation feasible.
128 Currently, many tidal studies have applied SAL treatment (Simmons et al., 2004; Schiller and
129 Fiedler, 2007; Griffies 2008; Arbic et al., 2010). η is the sea surface fluctuation and η_{tide} is the
130 instantaneous sea surface height due to equilibrium tides. \bar{P} represents the force from the
131 vertically integrated baroclinicity in the ocean columns, and the last term on the right side of the
132 equation (10) is the vertically integrated Coriolis force. τ_{tide} is a drag term, and includes
133 parameterized internal wave drag due to the oscillating flow over the topography and the wave
134 drag term due to the undulation of the sea surface (Jayne and Laurent, 2001; Simmons et al. 2004;
135 Schiller and Fiedler, 2007).

136 **3. Model description, numerical experimental design and data**

137 **3.1 Model**

138 The OGCM in this study is the second revised version of the LASG/IAP's (State Key
139 Laboratory of Numerical Modeling for Atmospheric Sciences and Geophysical Fluid
140 Dynamics/Institute of Atmospheric Physics) climate system ocean model (LICOM2.0) (Liu et al.,
141 2012; Dong et al., 2021), which adopts the free surface scheme in η -coordinate models and offers
142 the opportunity to explicitly resolve tides. The model domain is located between 78.5°S and
143 87.5°N with a 1° zonal resolution. The meridional resolution is refined to 0.5° between 10°S and
144 10°N and is increased gradually from 0.5° to 1° between 10° and 20°. There are 30 levels in the
145 vertical direction with 10m per layer in the upper 150m. Based on the original version of



146 LICOM2.0, key modifications have been made: (1) a new sea surface salinity boundary
147 condition was introduced that is based on the physical process of air–sea flux exchange at the
148 actual sea–air interface (Jin et al., 2017); (2) intra-daily air–sea interactions are resolved by
149 coupling the atmospheric and oceanic model components once every 2h; and (3) a new
150 formulation of the turbulent air–sea fluxes (Fairall et al., 2003) was introduced. The model has
151 been used as the ocean component model of the Chinese Academy of Sciences Earth System
152 Model (CAS-ESM 2.0) in its CMIP6 simulations (Zhang et al., 2020; Dong et al., 2021; Jin et al.,
153 2021).

154 **3.2 Numerical experimental design**

155 To investigate the effect of tidal processes on the simulation of the ocean climate, three sets
156 of experiments were conducted in the present study. The control experiment used the default
157 LICOM2.0 without tidal forcing (denoted as “CTRL” hereafter); Exp1 used the traditional
158 explicit tidal forcing formula of the eight most important constituents of the diurnal and
159 semidiurnal tides proposed by Griffies et al. (2009), and Exp2 used the new tidal forcing scheme.

160 For the control experiment, the Coordinated Ocean-ice Reference Experiments-I (CORE I)
161 protocol proposed by Griffies et al. (2009) was employed, and the repeating annual cycle of
162 climate atmospheric forcing from Large and Yeager (2004) was used. The model was firstly
163 spun up for 300 years in order to reach a quasi-equilibrium state. All three experiments started
164 from the quasi-equilibrium state (300th year) of the spin-up experiment and are integrated for 50
165 years under the same CORE I forcing fields. The diapycnal mixing of Laurent et al. (2002) and



166 Simmons et al. (2004) was also applied to the baroclinic momentum and tracer equations. The
167 hourly output of sea surface height in the last 10 years of the two tidal experiments was used to
168 conduct the harmonic analysis and obtain the spatial information of tidal constituents.

169 **3.3 Data**

170 TPXO9v2 is the assimilated data from a hydrodynamic model of the barotropic tides
171 constrained by a satellite altimetry (Egbert and Erofeeva, 2002). To verify the effect of the two
172 tidal schemes for high tidal amplitude regions, we also used two tidal stations, Yakutat (59.54°N,
173 139.73°W) and the Diego Ramirez Islands (56.56°S, 68.67°W), where the spectrum analysis was
174 carried out. The station observations are from the sea level Data Assembly Center (DAC) of the
175 World Ocean Circulation Experiment (WOCE) (Ponchaut et al., 2001). The data obtained from
176 the Archiving, Validation and Interpretation of Satellite Oceanographic data (AVISO)
177 (Schneider et al., 2013) are used in the observation of the dynamic sea level (DSL).

178 **4. Result**

179 **4.1 Tidal forcing**

180 Tides include spring tides, which are on the same line with the Sun, the Earth and the Moon,
181 and neap tides, which are when the Sun, the Earth and the Moon are not aligned. Figure 2 and
182 Figure 3 show the spatial distributions of spring and neap tidal height η_{tide} calculated by the two
183 tidal schemes. As expected, the two types of tides in Exp1 and Exp2 both have significant
184 diurnal variations and exhibit a phase shift from east to west (Fig. 2). Both experiments



185 simulated similar positions of the positive centers for spring tides, which are consistent with the
186 overlap of the projected positions of the Moon and the Sun. It is important to note that the
187 negative regions of the spring tide simulated in Exp2 exhibit large non-closed circular bands,
188 which represents the elliptic model of the equilibrium tide theory (Schwiderski, 1980), and this is
189 absent in Exp1 where the traditional explicit eight tidal constituents scheme is used.

190 There are pronounced differences in neap tides between Exp1 and Exp2 (Fig. 3). The neap
191 tide simulated in Exp2 shows a larger meridional variation. The positive regions are mainly
192 concentrated in the middle and low latitudes. The negative regions are mainly concentrated in the
193 high latitudes of the two hemispheres, which is due to less tidal forcing in the high latitudes
194 compared to the middle and low latitudes. This pattern of neap tide in Exp2 indicates that the
195 projection positions of both the Sun and Moon are located in the middle and low latitudes, which
196 is consistent with the results of Gill (2015). However, Exp1 presents a larger zonal variation
197 (positive-negative-positive-negative pattern), and the negative regions are concentrated in the
198 middle and low latitudes rather than the high latitudes, which implies that the projection position
199 of the Sun is located in the high latitudes. The different distributions of neap tides between Exp1
200 and Exp2 indicate that the new tidal formulation can better represent the position of the Sun
201 compared to the traditional scheme.

202 **4.2 Tidal constituents**

203 The harmonic analysis of the hourly sea surface height data simulated by the two tidal
204 schemes is carried out in order to obtain the amplitude and phase of each major tidal constituent.



205 TPXO9v2 is used as the observed data (Egbert and Erofeeva, 2002). In this study, we mainly
206 focus on the amplitudes and phases of the two largest constituents among the eight tidal
207 constituents, including a full diurnal constituent of K1 and a half-diurnal constituent of M2. To
208 quantitatively compare the simulations of tidal constituents by the two schemes, we calculated
209 the mean square error following Shriver et al. (2012):

$$total\ error^2 = \left[\frac{1}{2} (A_{model} - A_{TPXO})^2 \right] + [A_{model} A_{TPXO} (1 - \cos(\phi_{model} - \phi_{TPXO}))] \quad (11)$$

210 where A_{model} and A_{TPXO} are simulated and observed amplitudes, respectively, and ϕ_{model} and
211 ϕ_{TPXO} are simulated and observed phases, respectively. The total errors in each tidal constituent
212 can be divided into amplitude error and phase error; the former is the first term on the right side
213 of equation (11), and the latter is the second term on the right side of equation (11).

214 Figure 4 shows the respective amplitudes and phases of K1 for the observation, Exp1, and
215 Exp2, the total errors for the two experiments against the observation, and the difference in the
216 total errors between the two experiments. The amplitudes and phases of K1 simulated in both
217 Exp1 and Exp2 are similar to the observation (Fig. 4a–4c). The large values of the amplitudes of
218 K1 are located in the North Pacific Ocean, Indonesia, Ross Sea and Weddell Sea. However,
219 Exp1 simulated a larger amplitude of K1, and the extent of the large amplitude is too excessive,
220 especially for the North Pacific Ocean and Southern Ocean, compared to the extent of the large
221 amplitude in the observation and Exp2, which is consistent with the results of Yu et al. (2016).
222 The simulated amplitude of K1 by Exp2 is significantly improved and closer to the observation.



223 The global mean values of K1 are 11.58cm, 14.74cm and 10.50cm for the observation, Exp1 and
224 Exp2, respectively.

225 The total error patterns of K1 in Exp1 and Exp2 show a similar distribution (Fig. 4d and 4e);
226 large values are located in the Southern Ocean and the North Pacific. The total error of K1 in
227 Exp2 is smaller than in Exp1 in most regions except for the Arabian Sea, especially for the
228 Southern Ocean, the North Pacific and the eastern equatorial Pacific (Fig. 4f). The global mean
229 total errors of the K1 in Exp1 and Exp2 are 7.43cm and 6.28cm, respectively. According to
230 formula (11), the total error of K1 is divided into amplitude error and phase error (Fig. 5).
231 Compared with Exp1, the amplitude error of K1 is significantly improved in most regions,
232 especially for the large amplitude of K1 regions, which is the main reason for the smaller total
233 error of K1 in Exp2, although the phase error is also slightly reduced; this suggests that the new
234 tidal scheme leads to a better simulation of the amplitude and phase of K1, especially for the
235 amplitude simulation. The global mean of the amplitude errors in Exp1 and Exp2 are 4.97cm and
236 3.73cm, respectively, and the corresponding phase errors in both experiments are 5.52cm and
237 5.06cm, respectively.

238 M2 is known to be the largest tidal constituent (Griffies et al. 2009). Figure 6 shows the
239 respective amplitudes and phases of M2 for the observation, Exp1, and Exp2, as well as the total
240 errors for the two experiments against the observation and the difference in the total errors
241 between the two experiments. Both Exp1 and Exp2 can reasonably simulate the overall spatial
242 distribution patterns of M2's amplitude and phase (Fig. 6a–6c). The maximum values of the



243 amplitude are located in the Bay of Alaska, the eastern equatorial Pacific, Sman sea and the
244 North Atlantic. The amplitudes of M2 simulated in both Exp1 and Exp2 are larger than the
245 observation, especially for Ross Sea and Weddell Sea, though Exp2 exhibits some alleviation of
246 the bias when compared to Exp1. The global mean values of M2 are 33.30cm, 42.76cm and
247 38.29cm for the observation, Exp1 and Exp2, respectively.

248 The total error patterns of M2 in Exp1 and Exp2 also show similar features (Fig. 6d and 6e);
249 the large values are located in the large amplitude of M2 regions, noting the smaller magnitude
250 of the total error of M2 in Exp2 relative to Exp1 in most regions. The global mean of total error
251 in Exp2 (24.42cm) is obviously lower than in Exp1 (37.21cm). In addition, the amplitude error
252 and the phase error of M2 in Exp2 are both improved, the global mean of amplitude errors in
253 Exp1 and Exp2 are 14.77cm and 12.86cm, respectively, and the corresponding phase errors in
254 Exp1 and Exp2 are 34.16cm and 20.76cm, respectively. Inconsistent with K1, the smaller total
255 error of M2 in Exp2 relative to Exp1 is mainly the result of the phase error; in particular, the
256 phase errors of Exp2 are almost eliminated in the Indian Ocean and the Atlantic Ocean (Fig. 7).
257 This indicates the new tidal scheme results in the better simulation of M2, especially for the
258 phase simulation.

259 Furthermore, we also investigate the amplitudes and total errors of the remaining six tidal
260 constituents (O1, P1, Q1, S2, N2 and K2) simulated using two schemes. For amplitudes, the
261 global means of the three constituents (O1, P1 and K2) in Exp2 are closer to the observed values
262 relative to Exp1. The global mean observed values for the O1, P1, Q1, S2, N2 and K2 are



263 8.34cm, 3.62cm, 1.76cm, 13.35cm, 7.08cm and 3.75cm, respectively, and the corresponding
264 values in Exp1 (Exp2) are 10.59cm (9.79cm), 13.49cm (9.47cm), 1.62cm (2.19cm), 12.45cm
265 (9.85cm), 7.74cm (9.79cm) and 10.89cm (7.33cm), respectively (Table 1). For the total errors,
266 the global mean total errors for the remaining six constituents in Exp2 (with the exception of Q1
267 and N2) are smaller than those in Exp1, and the global mean total errors of the remaining six
268 constituents in Exp1 (Exp2) are 8.89cm (5.34cm), 9.53cm (6.26cm), 1.29cm (1.47cm), 11.26cm
269 (9.40cm), 5.84cm (6.76cm) and 10.32cm (6.55cm), respectively. Compared to Exp1, the
270 improved total errors of O1 and S2 in Exp2 are mainly the result of the smaller phase errors, and
271 the improvement of the total error of P1 in Exp2 is predominantly due to the lower amplitude
272 error. The global mean amplitude errors of O1, P1, S2, and K2 in Exp1 (Exp2) are 3.28cm
273 (3.16cm), 9.18cm (5.58cm), 5.11cm (5.68cm) and 6.50cm (3.72cm), respectively, and the
274 corresponding phase errors are 8.26cm (4.30cm), 2.57cm (2.84cm), 10.04cm (7.49cm) and
275 8.01cm (5.39cm), respectively (Table 1). The above results indicate that the new formulation of
276 the tidal scheme can better simulate more constituents of tides relative to the traditional method
277 of eight tidal constituents with empirical amplitudes and frequencies.

278 To further evaluate the simulation of the eight tidal constituents by using the two tidal
279 schemes, we also made a spectrum analysis at the Diego Ramirez Islands (56.56°S, 68.67°W)
280 and Yakutat (59.54°N, 139.73°W) tidal stations, which are located in regions with large tidal
281 amplitudes (Fig. 8). Both Exp1 and Exp2 can reasonably reproduce the amplitudes and
282 frequencies of the eight main tidal constituents at the Diego Ramirez Islands and Yakutat stations,



283 although most of the simulated amplitudes in Exp1 are much larger than the observed data. The
284 larger amplitude biases of the eight main tidal constituents at both stations (except for the Q1
285 constituent at the Diego Ramirez station) are all significantly improved in Exp2 (Table 2). For
286 instance, the amplitude of M2 in Exp1 at the Yakutat station is 141.58cm, and it is reduced to
287 130.65cm in Exp2, which is closer to the observed data (101.24cm). The amplitude of K1 in
288 Exp1 at the Diego Ramirez station is 26.13cm, and it is reduced to 17.59cm in Exp2, which is
289 closer to the observed data (18.82cm). On the basis of these preliminary evaluations, compared
290 to the traditional explicit eight tidal constituents scheme, the new tidal scheme can better
291 reproduce the spatial patterns of the amplitude of tidal constituents and tidal forcing, especially
292 for the magnitude of the amplitude.

293 **4.3 Dynamic sea level (DSL)**

294 Figure 9 shows the spatial distributions of DSL for the observation, CTRL and the bias in
295 CTRL, Exp1 and Exp2 relative to the observations as well as the difference between Exp2 and
296 Exp1. The observation is obtained from the Archiving, Validation and Interpretation of Satellite
297 Oceanographic data (AVISO) (Schneider et al., 2013). The DSL simulated by CTRL shows a
298 low DSL located in the Labrador Sea, the Nordic Seas and the Southern Ocean, and a high DSL
299 in the tropical and subtropical Pacific and Indian Oceans (Fig. 9b), which is consistent with the
300 observed data (Fig. 9a). Therefore, the ocean model, LICOM2.0, without a tidal process can
301 reproduce the basic pattern of DSL, but large biases also exist (Fig. 9c); there is a dipole pattern
302 bias located across the Antarctic Circumpolar Circulation (negative bias to the north and positive



303 bias to the south), a striking negative bias in the North Atlantic and a slightly positive bias in the
304 western equatorial Pacific.

305 The DSL in both Exp1 and Exp2 are improved and the striking negative bias for the North
306 Atlantic is reduced (Fig. 9d and 9e), which can be attributed to the improvement of the path of
307 the North Atlantic Gulf Stream due to the effects of tides, as pointed out by Müller et al. (2010).
308 There are some significant differences between Exp1 and Exp2. Compared to Exp1, Exp2
309 exhibits a striking latitudinal distribution feature (Fig. 9f), which shows a decreasing spatial
310 pattern from the equator to the poles, with positive values in the tropic region and a negative
311 pattern in high latitudes. This is because Exp2, in applying the new formulation of the tidal
312 scheme, can better represent the projection positions of both the Sun and Moon relative to Exp1.
313 Therefore, compared to Exp1, the positive bias in the Southern Ocean simulated by CTRL is
314 improved in Exp2, as exhibited by the negative difference between Exp2 and Exp1 at high
315 latitudes.

316 **5. Summary**

317 In this paper, a new explicit tidal scheme is introduced to a global ocean model. The scheme
318 uses the positional characteristics of the Moon and the Sun to calculate the tides directly instead
319 of applying empirical specifications, such as the amplitudes and frequencies of tides, which were
320 used in traditional methods. Compared with the traditional explicit eight tidal constituents
321 scheme, we found that the new tidal scheme can better simulate the spatial characteristics of
322 spring and neap tides. It significantly reduces the biases of larger amplitudes in the traditional



323 explicit tidal scheme, and better reproduces the spatial patterns of tidal constituents than the
324 traditional method. In theory, this scheme is also better suited than the traditional method to
325 simulate sea level height at regional scales which may not all be captured by the small number of
326 prescribed modes.

327 Furthermore, we study the total errors of the eight tidal constituents, including amplitude
328 errors and phase errors. The total errors of the eight tidal constituents simulated by the new tidal
329 scheme, with the exception of N2 and Q1, are all smaller than those simulated by the traditional
330 method. Compared to the traditional method, the improved total errors of M2, O1 and S2
331 simulated by the new tidal scheme are mainly the result of the better phase simulation (the
332 smaller phase errors); the reduction in the total errors of K1 and P1 are predominantly due to the
333 improvement in the amplitude simulation (with fewer amplitude errors); and the smaller total
334 error of K2 is associated with both the improvements in the amplitude and phase simulation
335 (both the smaller phase and amplitude errors).

336 The influence of tidal forcing on the simulation of DSL is also investigated. We found both
337 tidal schemes can significantly improve the simulation of DSL, and the striking negative bias for
338 the North Atlantic in CTRL is reduced. Compared with the traditional explicit eight tidal
339 constituents scheme, the new tidal scheme exhibits a latitudinal variation of DSL with a positive
340 difference in the tropics and a negative pattern in high latitudes, which improves the significant
341 positive bias of the Southern Ocean in CTRL.



342 It should be noted that the wave drag term formula proposed by Schiller and Fiedler (2007)
343 and the drag from internal wave generation (Jayne and Laurent, 2001; Simmons et al. 2004) are
344 adopted in the present study to decay the tidal energy, which is likely too strong in both tidal
345 experiments, especially with the traditional tidal forcing formula. Implementing a more
346 appropriate tidal drag parameterization in an OGCM still needs to be carried out. In addition, the
347 explicit introduction of tides into an OGCM is only a step towards upgrading ocean modeling. A
348 more detailed investigation into the impacts of the new tidal scheme on simulated ocean
349 circulations will be our future work, especially in an OCGM with a finer resolution and in a fully
350 coupled mode.

351 **Code availability.** *LICOM2.0 is the ocean component model of the Chinese Academy of Sciences*
352 *Earth System Model (CAS-ESM 2.0), which developed at IAP are intellectual property of IAP.*
353 *Permission to access the LICOM2.0 source code can be requested after contacting the*
354 *corresponding author (zqc@mail.iap.ac.cn) or Jiangbo Jin (jinjiangbo@mail.iap.ac.cn) and may*
355 *be granted after accepting the IAP Software License Agreement.*

356 **Data availability.** *TPXO9v2 is available from the following sources:*
357 *[https://doi.org/10.1175/1520-0426\(2002\)019<0183:EIMOBO>2.0.CO;2](https://doi.org/10.1175/1520-0426(2002)019<0183:EIMOBO>2.0.CO;2) (Egbert and Erofeeva,*
358 *2002). The station observations are from the sea level Data Assembly Center (DAC):*
359 *[https://doi.org/10.1175/1520-0426\(2001\)018<0077:AAOTTS>2.0.CO;2](https://doi.org/10.1175/1520-0426(2001)018<0077:AAOTTS>2.0.CO;2) (Ponchaut et al., 2001).*
360 *The observation of the DSL is available from the Archiving, Validation and Interpretation of*



361 *Satellite Oceanographic data (AVISO): <https://doi.org/10.1002/2013EO130001> (Schneider et al.,*
362 *2013).*

363 **Author contributions.** *QZ and JJ pondered the rationale of the method. JJ designed the*
364 *experiments. RG developed the model code and performed the simulations. JJ, MZ and RG*
365 *prepared the manuscript with contributions from all co-authors. MZ and GZ carried out*
366 *supervision.*

367 **Acknowledgments.** *This work is jointly supported by the National Natural Science Foundation of*
368 *China (Grant No 41991282), the Key Research Program of Frontier Sciences, the Chinese*
369 *Academy of Sciences (Grant No. ZDBS-LY-DQC010), the Strategic Priority Research Program*
370 *of the Chinese Academy of Sciences (Grant No. XDB42000000) and the open fund of the State*
371 *Key Laboratory of Satellite Ocean Environment Dynamics, Second Institute of Oceanography*
372 *(Grant No. QNHX2017). The simulations were performed on the supercomputers provided by the*
373 *Earth System Science Numerical Simulator Facility (EarthLab).*



374 **REFERENCES**

- 375 Arbic, B. K., Wallcraft, A. J., and Metzger, E. J.: Concurrent simulation of the eddy general
376 circulation and tides in a global ocean model, *Ocean Modell*, 32(3–4), 175–187,
377 <https://doi.org/10.1016/j.ocemod.2010.01.007>, 2010.
- 378 Dong, X., Jin, J., Liu, H., Zhang, H., Zhang, M., Lin, P., Zeng, Q., Zhou, G., Yu, Y., Song, Lin,
379 M., Z., Lian, R., Gao, X., He, J., Zhang, D., and Chen, K.: CAS-ESM2.0 model datasets for
380 the CMIP6 Ocean Model Intercomparison Project Phase 1 (OMIP1), *Adv. Atmos. Sci.*, 38,
381 307–316, <https://doi.org/10.1007/s00376-020-0150-3>, 2021.
- 382 Egbert, G. D., and Erofeeva, S. Y.: Efficient Inverse Modeling of Barotropic Ocean Tides, *J.*
383 *Atmos. Ocean. Tech.*, 19(2), 183–204, [https://doi.org/10.1175/1520-](https://doi.org/10.1175/1520-0426(2002)019<0183:EIMOBO>2.0.CO;2)
384 [0426\(2002\)019<0183:EIMOBO>2.0.CO;2](https://doi.org/10.1175/1520-0426(2002)019<0183:EIMOBO>2.0.CO;2), 2002.
- 385 Egbert, G. D., and Ray, R. D.: Semi-diurnal and diurnal tidal dissipation from TOPEX/Poseidon
386 altimetry, *Geophys. Res. Lett.*, 30(17), 169–172, <https://doi.org/10.1029/2003GL017676>,
387 2003.
- 388 Fairall, C. W., Bradley, E. F., Hare, J. E., Grachev, A. A., and Edson, J. B.: Bulk
389 parameterization of air–sea fluxes: Updates and verification for the COARE algorithm, *J.*
390 *Climate*, 16, 571–591, 2003.
- 391 Gill, S.: Sea-level science: Understanding tides, surges, tsunamis and mean sea-level changes,
392 *Phys Today*, 68, 56–57, 2015.



- 393 Griffies, S. M., and Adcroft, A. J.: Formulating the Equations of Ocean Models, *J. Geophys. Res.*,
394 177, 281–317, <https://doi.org/10.1029/177GM18>, 2008.
- 395 Griffies, S. M., Harrison, M. J., Pacanowski, R. C., and Rosati, A.: A Technical Guide to MOM4,
396 GFDL Ocean group Tech. Rep, 5, 309–313, 2004.
- 397 Griffies, S. M., Schmidt, M., and Herzfeld, M.: Elements of mom4p1, GFDL Ocean Group Tech.
398 Rep, 6, 444.p, 2009.
- 399 Hendershott, M. C.: The effects of solid earth deformation on global ocean tides, *Geophys J Int*,
400 29(4), 389–402, <https://doi.org/10.1111/j.1365-246X.1972.tb06167.x>, 1972.
- 401 Huang, R. X.: Mixing and energetics of the oceanic thermohaline circulation, *J. Phys. Oceanogr.*,
402 29, 727–746, 1999.
- 403 Jayne, S. R. and Laurent, L. C. S.: Parameterizing tidal dissipation over rough topography,
404 *Geophys. Res. Lett.*, 28(5), 811–814, <https://doi.org/10.1029/2000GL012044>, 2001.
- 405 Jin, J. B., Zeng, Q. C., Wu, L., Liu, H. L., and Zhang, M. H.: Formulation of a new ocean salinity
406 boundary condition and impact on the simulated climate of an oceanic general circulation
407 model, *Sci. China Earth Sci.*, 60, 491–500, <https://doi.org/10.1007/s11430-016-9004-4>, 2017.
- 408 Jin, J. B., Zhang, H., Dong, X., Liu, H. L., Zhang, M. H., Gao, X., He, J. X., Chai, Z. Y., Zeng, Q.
409 C., Zhou, G. Q., Lin, Z. H., Yu, Y., Lin, P. F., Lian, R. X., Yu, Y. Q., Song, M. R., and
410 Zhang, D. L.: CAS-ESM2.0 model datasets for the CMIP6 Flux-Anomaly-Forced Model
411 Intercomparison Project (FAFMIP), *Adv. Atmos. Sci.*, 38(2), 296–306,
412 <https://doi.org/10.1007/s00376-020-0188-2>, 2021.



- 413 Killworth, P. D., Stainforth, D., Webb, D. J., and Paterson, S. M.: The development of a free-
414 surface Bryan–Cox–Semtner ocean model, *J. Phys. Oceanogr.*, 21, 1333–1348, 1991.
- 415 Large, W. G., and Yeager, S.: Diurnal to decadal global forcing for ocean and sea–ice models:
416 the datasets and flux climatologies, NCAR Technical Note (No. NCAR/TN-460+STR),
417 <https://doi.org/10.5065/D6KK98Q6>, 2004.
- 418 Laurent, L. C. St., Simmons, H. L., and Jayne, S. R.: Estimating tidally driven mixing in the deep
419 ocean, *Geophys. Res. Lett.*, 29(23), 211–214, <https://doi.org/10.1029/2002GL015633>, 2002.
- 420 Liu, H. L., Lin, P. F., Yu, Y. Q., and Zhang, X. H.: The baseline evaluation of LASG/IAP
421 climate system ocean model (LICOM) version 2, *Acta Meteorol. Sin.*, 26, 318–329,
422 <https://doi.org/10.1007/s13351-012-0305-y>, 2012.
- 423 MacKinnon, J.: Mountain waves in the deep ocean, *Nature*, 501, 321–322,
424 <https://doi.org/10.1038/501321a>, 2013.
- 425 Melet, A., Hallberg, R., Legg, S., and Polzin, K.: Sensitivity of the ocean state to the vertical
426 distribution of internal-tide driven mixing, *J. Phys. Oceanogr.*, 43(3), 602–615,
427 <https://doi.org/10.1175/JPO-D-12-055.1>, 2013.
- 428 Montenbruck, and Gill.: Sun and moon, *Satellite Orbits: Models, Methods and Applications*, 69–
429 77, 2000.
- 430 Munk, W. and Wunsch, C.: Abyssal recipes II: energetics of tidal and wind mixing, *Deep Sea*
431 *Res. Part I Oceanogr. Res. Pap.*, 45(12), 1977–2010, [https://doi.org/10.1016/S0967-](https://doi.org/10.1016/S0967-0637(98)00070-3)
432 [0637\(98\)00070-3](https://doi.org/10.1016/S0967-0637(98)00070-3), 1998.



- 433 Müller, M., Haak, H., Jungclaus, J. H., Sündermann, J., and Thomas, M.: The effect of ocean
434 tides on a climate model simulation, *Ocean Modell*, 35(4), 304–313,
435 <https://doi.org/10.1016/j.ocemod.2010.09.001>, 2010.
- 436 Ponchaut, F., Lyard, F., and Provost, C. L.: An analysis of the tidal signal in the WOCE sea level
437 dataset, *J. Atmos. Ocean. Tech.*, 18(1), 77–91, [https://doi.org/10.1175/1520-0426\(2001\)018<0077:AAOTTS>2.0.CO;2](https://doi.org/10.1175/1520-0426(2001)018<0077:AAOTTS>2.0.CO;2), 2001.
- 439 Postlethwaite, C. F., Morales Maqueda, M. A., le Fouest, V., Tattersall, G. R., Holt, J. T., and
440 Willmott, A. J.: The effect of tides on dense water formation in Arctic shelf seas, *Ocean Sci.*,
441 7, 203–217, <https://doi.org/10.5194/os-7-203-2011>, 2011.
- 442 Saenko, O. A. and Merryfield, W. J.: On the effect of topographically enhanced mixing on the
443 global ocean circulation, *J. Phys. Oceanogr.*, 35, 826–834, 2005.
- 444 Schiller, A.: Effects of explicit tidal forcing in an OGCM on the water-mass structure and
445 circulation in the Indonesian throughflow region, *Ocean Modell*, 6(1), 31–49,
446 [https://doi.org/10.1016/S1463-5003\(02\)00057-4](https://doi.org/10.1016/S1463-5003(02)00057-4), 2004.
- 447 Schiller, A., and Fiedler, R.: Explicit tidal forcing in an ocean general circulation model,
448 *Geophys. Res. Lett.*, 34(3), L03611, <https://doi.org/10.1029/2006GL028363>, 2007.
- 449 Schneider, D. P., Deser, C., Fasullo, J., and Trenberth, K. E.: Climate data guide spurs discovery
450 and understanding, *Eos Trans. AGU*, 94(13), 121, <https://doi.org/10.1002/2013EO130001>,
451 2013.



- 452 Schwiderski, E.: On charting global ocean tides, *Rev. Geophys.*, 18(1), 243–268,
453 <https://doi.org/10.1029/RG018i001p00243>, 1980.
- 454 Shriver, J. F., Arbic, B. K., Richman, J. G., Ray, R. D., Metzger, E. J., Wallcraft, A. J., and
455 Timko, P. G.: An evaluation of the barotropic and internal tides in a high-resolution global
456 ocean circulation model, *J. Geophys. Res.*, 117, C10024,
457 <https://doi.org/10.1029/2012JC008170>, 2012.
- 458 Shum, C. K., Woodworth, P. L., Andersen, O. B., Egbert, G. D., Francis, O., King, C., Klosko, S.
459 M., Provost, C. L., Li, X., Molines, J. M., Parke, M. E., Ray, R. D., Schlax, M. G., Stammer,
460 D., Tierney, C. C., Vincent, P., and Wunsch, C. I.: Accuracy assessment of recent ocean tide
461 models, *J. Geophys. Res.*, 102(C11), 25173–25194, <https://doi.org/10.1029/97JC00445>,
462 1997.
- 463 Simmons, H. L., Jayne, S. R., Laurent, L. C. S., and Weaver, A. J.: Tidally driven mixing in a
464 numerical model of the ocean general circulation, *Ocean Modell.*, 6, 245–263,
465 [https://doi.org/10.1016/S1463-5003\(03\)00011-8](https://doi.org/10.1016/S1463-5003(03)00011-8), 2004.
- 466 Thomas, M., Sündermann, J., and Maier-Reimer, E.: Consideration of ocean tides in an OGCM
467 and impacts on subseasonal to decadal polar motion excitation, *Geophys. Res. Lett.*, 28(12),
468 2457–2460, <https://doi.org/10.1029/2000GL012234>, 2001.
- 469 Wahr, J. M. and Sasao, T.: A diurnal resonance in the ocean tide and in the earth load response
470 due to the resonant free “core nutation”, *Geophys. J. Int.*, 64(3), 747–765,
471 <https://doi.org/10.1111/j.1365-246X.1981.tb02693.x>, 1981.



- 472 Wang, X., Liu, Z., and Peng, S.: Impact of tidal mixing on water mass transformation and
473 circulation in the south china sea, *J. Phys. Oceanogr.*, 47(2), 419–432,
474 <https://doi.org/10.1175/JPO-D-16-0171.1>, 2017.
- 475 Wilmes, S. B., Schmittner, A., and Green, J. A. M.: Glacial Ice Sheet Extent Effects on Modeled
476 Tidal Mixing and the Global Overturning Circulation, *Paleoceanogr. Paleoclimatol.*, 34,
477 1437–1454, <https://doi.org/10.1029/2019PA003644>, 2019.
- 478 Wunsch, C., and Ferrari, R.: Vertical mixing, energy, and the general circulation of the oceans,
479 *Annu. Rev. Fluid Mech.*, 36, 281–314, 2004.
- 480 Yu, Y., Liu, H., and Lan, J.: The influence of explicit tidal forcing in a climate ocean circulation
481 model, *Acta Meteorol. Sin.*, 35(9), 42–50, <https://doi.org/10.1007/s13131-016-0931-9>, 2016.
- 482 Yu, Z., Liu, H., and Lin, P.: A Numerical Study of the Influence of Tidal Mixing on Atlantic
483 Meridional Overturning Circulation (AMOC) Simulation, *Chinese J. Atmospheric Sci.*,
484 41(5), 1087–1100, 2017.
- 485 Zhang, H., Zhang, M., Jin, J., Fei, K., Ji, D., Wu, C., Zhu, J., He, J., Chai, Z., Xie, J., Dong, X.,
486 Zhang, D., Bi, X., Cao, H., Chen, H., Chen, K., Chen, X., Gao, X., Hao, H., Jiang, J., Kong,
487 X., Li, S., Li, Y., Lin, P., Lin, Z., Liu, H., Liu, X., Shi, Y., Song, M., Wang, H., Wang, T.,
488 Wang, X., Wang, Z., Wei, Y., Wu, B., Xie, Z., Xu, Y., Yu, Y., Yuan, L., Zeng, Q., Zeng, X.,
489 Zhao, S., Zhou, G., Zhu, J.: Description and climate simulation performance of CAS-ESM
490 version 2, *J. Adv. Model. Earth. Sy.*, 12, e2020MS002210,
491 <https://doi.org/10.1029/2020MS002210>, 2020.



- 492 Zhang, R. H., and Endoh, M.: A free surface general circulation model for the tropical Pacific
493 Ocean, *J. Geophys. Res.*, 97(C7), 11237–11255, <https://doi.org/10.1029/92JC00911>, 1992.
- 494 Zhang, X., and Liang, X.: A numerical world ocean general circulation model. *Adv. Atmos. Sci.*,
495 6(1), 44–61, 1989.
- 496 Zhou, X. B., Zhang, Y. T., and Zeng, Q. C.: The interface wave of thermocline excited by the
497 principal tidal constituents in the Bohai Sea, *Acta Meteorol. Sin.*, 24(2), 20–29, 2002.



498 **Figure Captions**

499 **Figure 1.** Schematic of the tidal forces generated by the Moon, where M_m , a , D_m , and L are the
500 Moon, the radius of the Earth, the distance to the Moon, and the distance of the Moon from any
501 point X on the Earth, respectively. θ_m is the zenith angle of point X relative to the Moon, and r is
502 the angle between the Moon pointing to the center of the Earth and point X.

503

504 **Figure 2.** Spatial patterns of the spring tides for Exp1 (the first column) and Exp2 (the second
505 columns), and the interval between the row is six hours. The units are cm.

506

507 **Figure 3.** Spatial patterns of the neap tides for Exp1 (the first column) and Exp2 (the second
508 columns), and the interval between the row is six hours. The units are cm.

509

510 **Figure 4.** Spatial patterns of the amplitude and phase of K1 for (a) the observation (Obs), (b)
511 Exp1, (c) Exp2, (d) the total error for Exp1, (e) the total error for Exp2, and (f) the difference in
512 error between Exp2 and Exp1. The observation is from TPXO9v2 (Egbert and Erofeeva, 2002).
513 The units are cm, and the lines of the constant phase are plotted every 45° in black.

514

515 **Figure 5.** The contributions to the total error of K1 resulting from errors in (a) tidal amplitude
516 and (b) phase for Exp1; (c) and (d) are the same as above, but for Exp2. The units are cm.

517



518 **Figure 6.** Spatial patterns of the amplitude and phase of M2 for (a) the observation (Obs), (b)
519 Exp1, (c) Exp2, (d) the total error for Exp1, (e) the total error for Exp2, and (f) the difference in
520 error between Exp2 and Exp1. The observation is from TPXO9v2 (Egbert and Erofeeva, 2002).
521 The units are cm, and the lines of the constant phase are plotted every 45° in black.

522

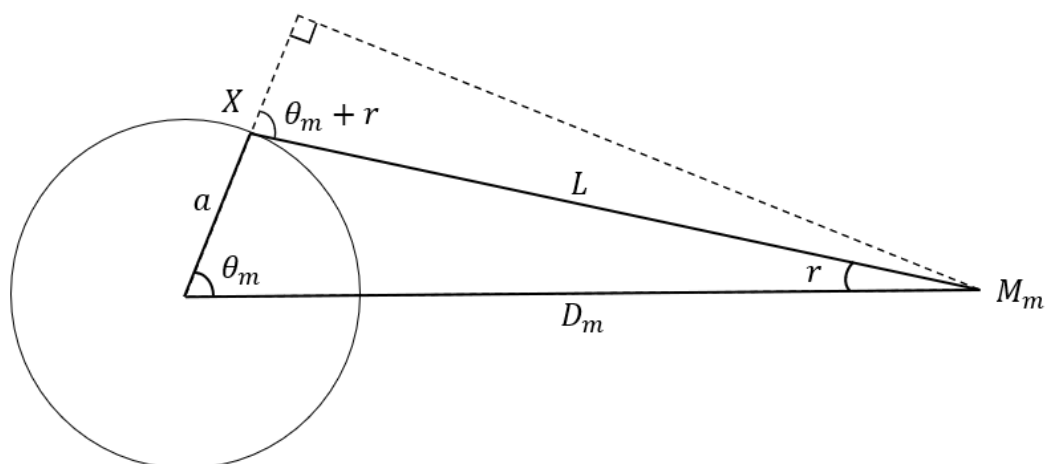
523 **Figure 7.** The contributions to the total error of M2 resulting from errors in (a) tidal amplitude
524 and (b) phase for Exp1; (c) and (d) are the same as above, but for Exp2. The units are cm.

525

526 **Figure 8.** Spectrum analysis of sea surface height for (a) the observation (Obs), (b) Exp1, and (c)
527 Exp2, and (d–f) is the same as above. The observation is from WOCE (Ponchaut et al., 2001).
528 The upper panels are for the Diego Ramirez Islands (56.56°S, 68.67°W) and the lower panels are
529 for Yakutat (59.54°N, 139.73°W).

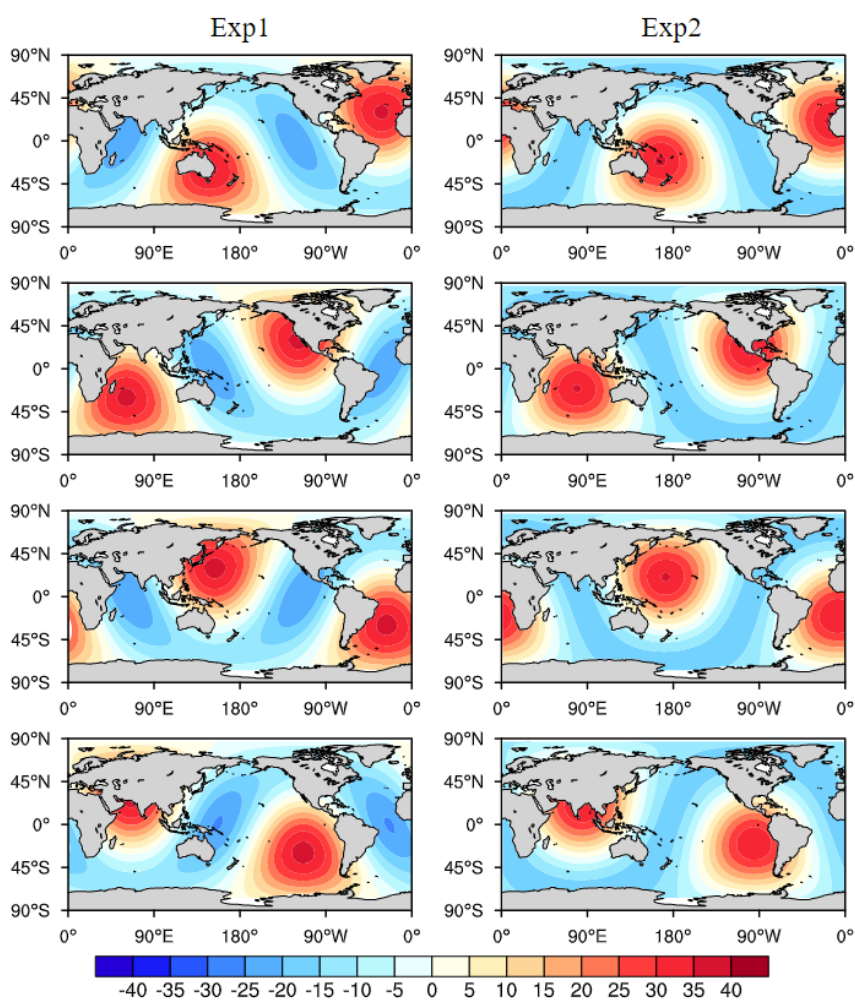
530

531 **Figure 9.** Spatial patterns of the dynamic sea level for (a) the observation (Obs), (b) CTRL, (c)
532 the difference between CTRL and observation, (d) the difference between Exp1 and CTRL, (e)
533 the difference between Exp2 and CTRL, and (f) the difference between Exp2 and Exp1. The
534 observation is from AVISO (Schneider et al., 2013), and the units are m.



535

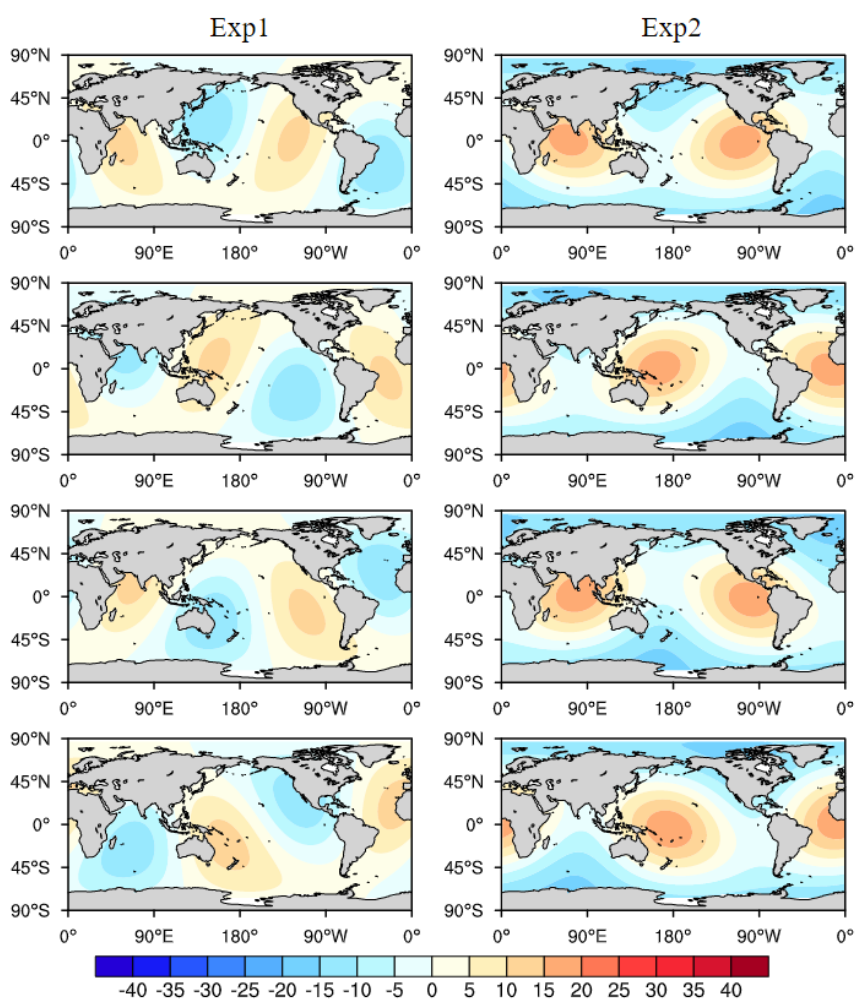
536 **Figure 1.** Schematic of the tidal forces generated by the Moon, where M_m , a , D_m , and L are the
537 Moon, the radius of the Earth, the distance to the Moon, and the distance of the Moon from any
538 point X on the Earth, respectively. θ_m is the zenith angle of point X relative to the Moon, and r is
539 the angle between the Moon pointing to the center of the Earth and point X.



540

541 **Figure 2.** Spatial patterns of the spring tides for Exp1 (the first column) and Exp2 (the second

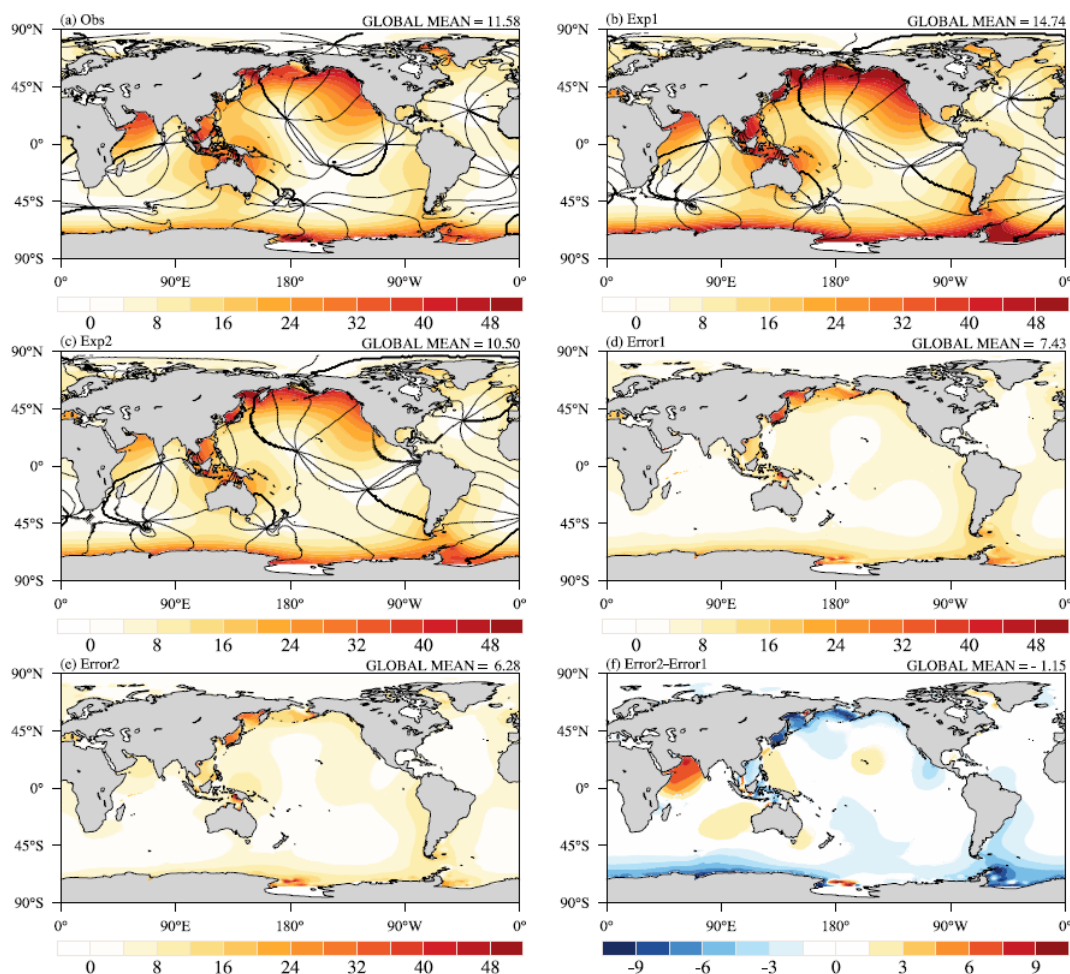
542 columns), and the interval between the row is six hours. The units are cm.



543

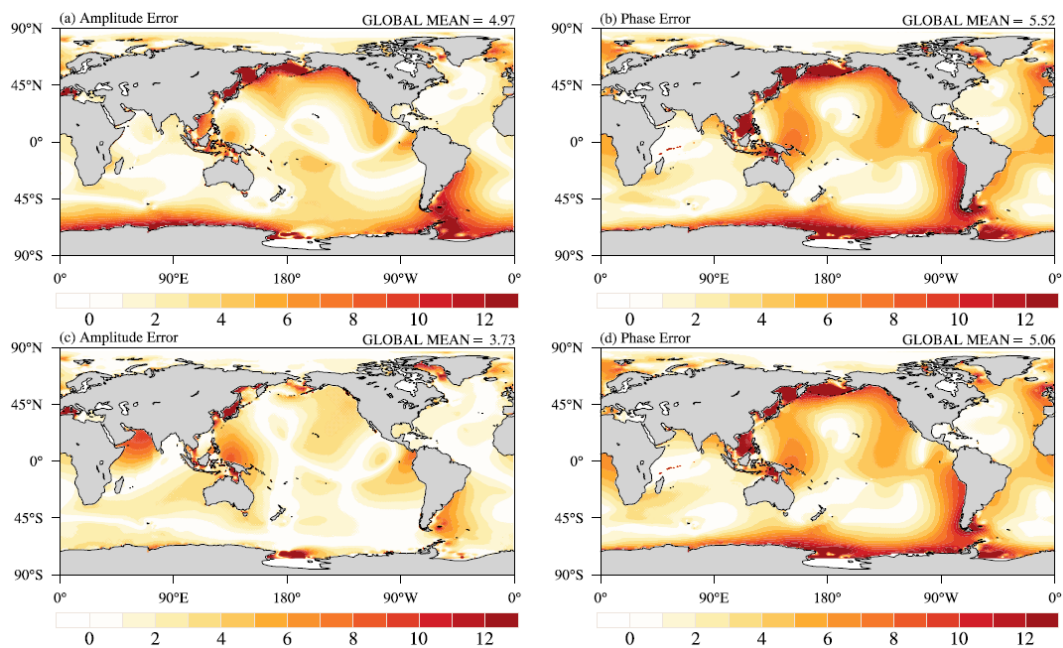
544 **Figure 3.** Spatial patterns of the neap tides for Exp1 (the first column) and Exp2 (the second

545 columns), and the interval between the row is six hours. The units are cm.



546

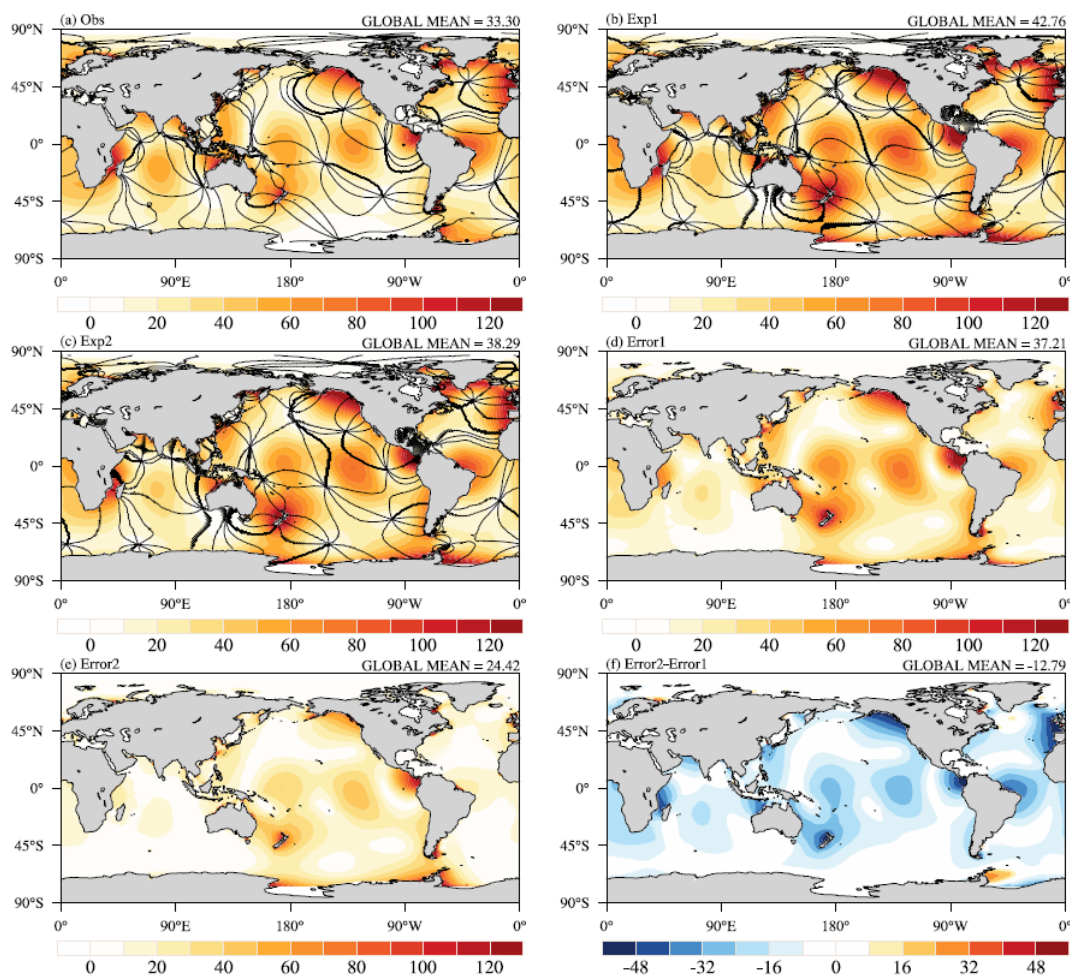
547 **Figure 4.** Spatial patterns of the amplitude and phase of K1 for (a) the observation (Obs), (b)
548 Exp1, (c) Exp2, (d) the total error for Exp1, (e) the total error for Exp2, and (f) the difference in
549 error between Exp2 and Exp1. The observation is from TPXO9v2 (Egbert and Erofeeva, 2002).
550 The units are cm, and the lines of the constant phase are plotted every 45° in black.



551

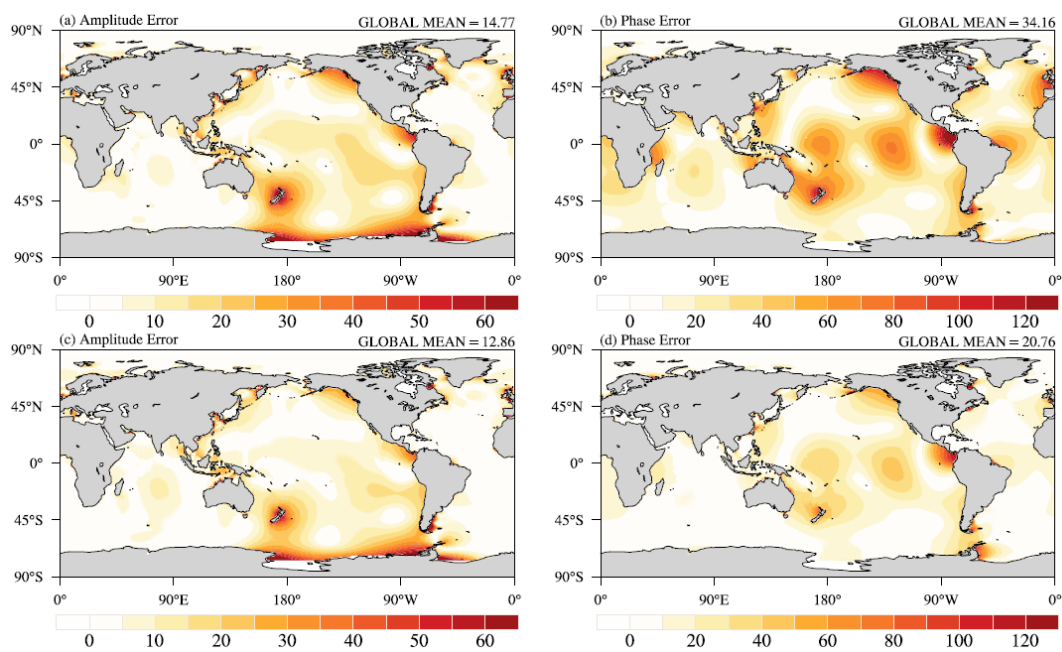
552 **Figure 5.** The contributions to the total error of K1 resulting from errors in (a) tidal amplitude

553 and (b) phase for Exp1; (c) and (d) are the same as above, but for Exp2. The units are cm.



554

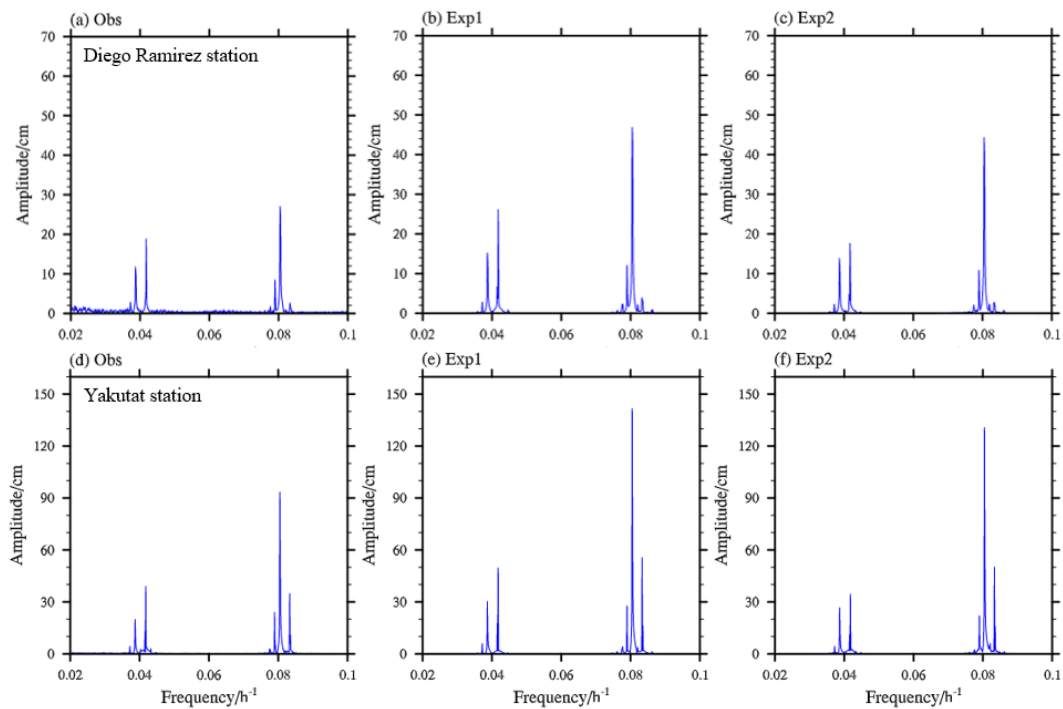
555 **Figure 6.** Spatial patterns of the amplitude and phase of M2 for (a) the observation (Obs), (b)
556 Exp1, (c) Exp2, (d) the total error for Exp1, (e) the total error for Exp2, and (f) the difference in
557 error between Exp2 and Exp1. The observation is from TPXO9v2 (Egbert and Erofeeva, 2002).
558 The units are cm, and the lines of the constant phase are plotted every 45° in black.



559

560 **Figure 7.** The contributions to the total error of M2 resulting from errors in (a) tidal amplitude

561 and (b) phase for Exp1; (c) and (d) are the same as above, but for Exp2. The units are cm.

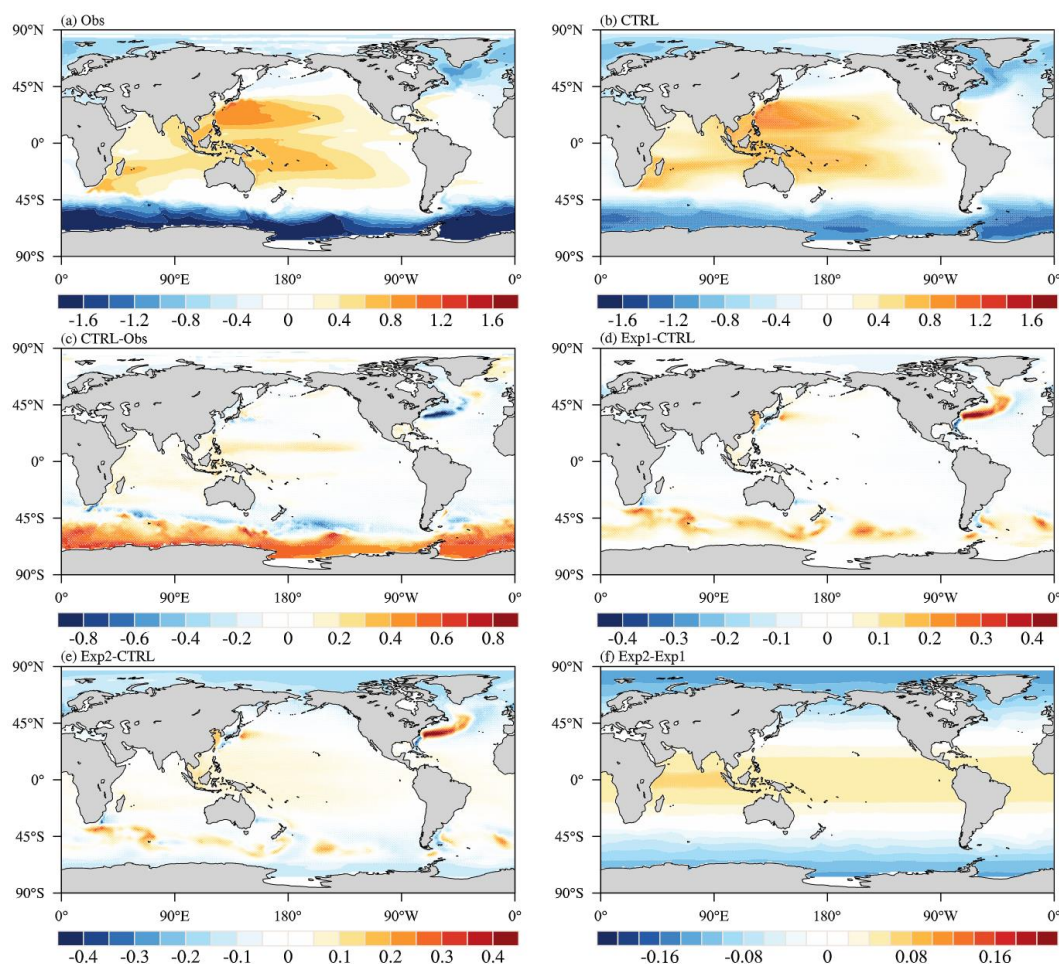


562

563 **Figure 8.** Spectrum analysis of sea surface height for (a) the observation (Obs), (b) Exp1, and (c)
564 Exp2, and (d–f) is the same as above. The observation is from WOCE (Ponchaut et al., 2001).

565 The upper panels are for the Diego Ramirez Islands (56.56°S, 68.67°W) and the lower panels are

566 for Yakutat (59.54°N, 139.73°W).



567

568 **Figure 9.** Spatial patterns of the dynamic sea level for (a) the observation (Obs), (b) CTRL, (c)

569 the difference between CTRL and observation, (d) the difference between Exp1 and CTRL, (e)

570 the difference between Exp2 and CTRL, and (f) the difference between Exp2 and Exp1. The

571 observation is from AVISO (Schneider et al., 2013), and the units are m.

572



573 **Table Captions**

574 **Table 1.** Global mean values of the amplitudes of the eight tidal constituents during observation,
575 Exp1 and Exp2, and the amplitude, phase, and total errors of the eight tidal constituents in Exp1
576 and Exp2. The units are cm. The better amplitude and lower errors in Exp2 relative to Exp1 are
577 marked by bold font.

578

579 **Table 2.** The amplitudes of the eight tidal constituents during the observation (Obs), Exp1 and
580 Exp2 at the Diego Ramirez Islands (56.56°S, 68.67°W) and Yakutat (59.54°N, 139.73°W). The
581 observation is from WOCE (Ponchaut et al., 2001), and the units are cm. The better amplitude in
582 Exp2 relative to Exp1 is marked by bold font.

583



584 **Table 1.** Global mean values of the amplitudes of the eight tidal constituents during observation,
 585 Exp1 and Exp2, and the amplitude, phase, and total errors of the eight tidal constituents in Exp1
 586 and Exp2. The units are cm. The better amplitude and lower errors in Exp2 relative to Exp1 are
 587 marked by bold font.

	Global mean			Amplitude Error		Phase Error		Total Error	
	Obs	Exp1	Exp2	Exp1	Exp2	Exp1	Exp2	Exp1	Exp2
M2	33.30	42.76	38.29	14.77	12.86	34.16	20.76	37.21	24.42
S2	13.35	12.45	9.85	5.11	5.68	10.04	7.49	11.26	9.40
N2	7.08	7.74	9.79	2.20	3.34	5.41	5.88	5.84	6.76
K2	3.75	10.89	7.33	6.50	3.72	8.01	5.39	10.32	6.55
K1	11.58	14.74	10.50	4.97	3.73	5.52	5.06	7.43	6.28
O1	8.34	10.59	9.79	3.28	3.16	8.26	4.30	8.89	5.34
P1	3.62	13.49	9.47	9.18	5.58	2.57	2.84	9.53	6.26
Q1	1.76	1.62	2.19	0.57	0.76	1.16	1.26	1.29	1.47



588 **Table 2.** The amplitudes of the eight tidal constituents during the observation (Obs), Exp1 and
 589 Exp2 at the Diego Ramirez Islands (56.56°S, 68.67°W) and Yakutat (59.54°N, 139.73°W). The
 590 observation is from WOCE (Ponchaut et al., 2001), and the units are cm. The better amplitude in
 591 Exp2 relative to Exp1 is marked by bold font.

	Diego Ramirez			Yakubu		
	Obs	Exp1	Exp2	Obs	Exp1	Exp2
M2	27.01	46.84	44.28	101.24	141.58	130.65
S2	2.62	3.93	2.73	35.61	55.49	50.05
N2	8.49	12.10	10.84	24.48	27.71	22.04
K2	1.15	2.94	2.12	9.34	16.28	15.71
K1	18.82	26.13	17.59	39.33	49.53	34.37
O1	11.73	15.20	13.83	20.53	30.18	26.55
P1	3.75	6.66	4.80	11.94	17.70	11.05
Q1	2.82	2.81	2.28	2.79	5.96	4.37

592